Results in Materials 29 (2026) 100882

Contents lists available at ScienceDirect

Results in Materials

journal homepage: www.sciencedirect.com/journal/results-in-materials

DFT study of structural, mechanical, electronic, and thermoelectric properties of $YNbNi_2X_2$ (X=Si or Ge) double half-Heusler alloy

Job W. Wafula [a],*, George S. Manyali [b], John W. Makokha [a]

[a] Department of Physics, Kibabii University, 1699-50200, Bungoma, Kenya
[b] Computational and Theoretical Physics Group (CTheP), Department of Physical Sciences, Kaimosi Friends University, 385-50309, Kaimosi, Kenya

ARTICLE INFO

Keywords:
Double half-Heusler
$YNbNi_2Si_2$
$YNbNi_2Ge_2$
Thermoelectrics
Density functional theory

ABSTRACT

This work examines the structural, mechanical, electronic, and thermoelectric characteristics of $YNbNi_2X_2$ (X = Si, Ge) double half-Heusler alloys using density functional theory (DFT) computations. Thermodynamic stability was demonstrated by formation energy estimates, and mechanical parameters show ductile behavior with good mechanical stability. $YNbNi_2Si_2$ and $YNbNi_2Ge_2$ exhibit semiconducting characteristics, with indirect band gaps of 0.51 eV and 0.56 eV, respectively. The Boltzmann transport equation is used to investigate thermoelectric properties, which yield promising Seebeck coefficients and electrical conductivities. The dimensionless figure of merit (ZT) for $YNbNi_2Ge_2$ and $YNbNi_2Si_2$ peaks at 0.85 and 0.68 at 300 K respectively. However, these values should be regarded as upper limits, as only the electronic contribution to thermal conductivity was considered, and the lattice contribution was not explicitly calculated. The figure of merit (ZT) increases with temperature suggesting that these are potential materials for energy harvesting applications at high temperature.

1. Introduction

Thermoelectrics and optoelectronics are crucial materials for reforming the advanced technologies such as photovoltaic and thermoelectricity which are potential technologies that provide means of generating clean energy [1,2]. Half-Heusler (HH) alloys are high-performance thermoelectric (TE) materials because of their high Seebeck coefficient, however, they suffer from intrinsic high thermal conductivity [3–8]. ZrCoBi, a high performance half-Heusler alloy, has the lowest recorded lattice thermal conductivity of 10 W/(m K) at 300 K [9]. Alloys are characterized by their valence electron count (VEC); for instance, HH alloys with 18 valence electrons exhibit high stability due to their fully occupied bonding and empty anti-bonding states. Erden Gulebaglan and Kilit Dogan (2021) found that 17 and 19 valence-electron HH alloys are unstable due to their partly occupied condition [10,11]. Guo et al. (2020) found that combining a 17 and 19 VEC HH alloy can result in an 18 VEC double half-Heusler alloy [12]. The combination effectively scatters phonons, lowering lattice thermal conductivity, and boosting thermoelectric performance. According to Anand et al. (2019), double half-Heusler alloys have much lower lattice thermal conductivity than their ternary counterparts [13]. The electrical transport capabilities of double HH alloys may outperform those of ternary systems, which makes them interesting for TE applications [14]. Numerous undiscovered double half-Heusler alloys were predicted and proved to be stable. Previous investigations show that the thermal conductivity of the double half-Heusler $Ti_2FeNiSb_2$ is lower than that of the high-performance ternary TiCoSb alloy (which satisfies the 18-valence-electron rule, ΔVEC = 0) [13]. Alloying the two phases can result in solid solutions at high temperatures and ordered structures at low temperatures. Alloying solid solutions at high temperatures has been used to lower thermal conductivity, although it can affect carrier mobility [12]. Zhang et al. (2013) found that an ordered structure with low heat conductivity may maintain high weighted mobility [15]. Research indicates that half-Heusler compounds' thermoelectric performance is influenced by their electronic structure [16–18]. Electronic structures and electrical transport computations show that $Ti_4Fe_2Ni_2Sb_4$ and $V_4Fe_2Ni_2Ge_4$ have better p- and n-type electrical properties than equivalent solid solutions due to bigger DOS but lighter band effective masses. At high temperatures, the combination of two phases results in a solid solution, whereas at low temperature it forms an ordered structure. $Ti_4Fe_2Ni_2Sb_4$ and $V_4Fe_2Ni_2Ge_4$ have projected n-type (p-type) ZT values of 1.75 (0.64) and 1.33 (0.95), respectively. According to Guo et al. (2020), creating structured structures rather than solid solutions can lead to superior thermoelectric characteristics in double HH systems [12]. In this study, the structural, mechanical, electronic and thermoelectric properties of $YNbNi_2Si_2$ and $YNbNi_2Ge_2$ double half-Heusler alloys were investigated using density functional theory (DFT) implemented in the Quantum ESPRESSO routine [19]. There are no

* Corresponding author.
E-mail address: jobwafula691@gmail.com (J.W. Wafula).

https://doi.org/10.1016/j.rinma.2025.100882
Received 13 May 2025; Received in revised form 24 November 2025; Accepted 28 December 2025
Available online 30 December 2025

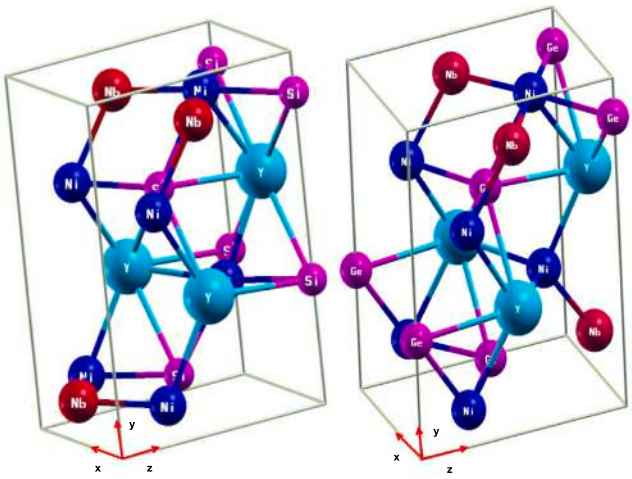

Fig. 1. The unit cells of $YNbNi_2Si_2$ and $YNbNi_2Ge_2$ double half-Heusler alloys.

reported calculated phases of $YNbNi_2Si_2$ and $YNbNi_2Ge_2$ double half-Heusler alloys but their formation enthalpy per atom (ΔH_f= −0.774 eV/atom and −0.657 eV/atom receptively [20,21]) demonstrates that the alloys are stable thermodynamically.

2. Computational details

The density functional theory (DFT) within the Quantum ESPRESSO code [19], along with the Thermo_pw code the structural, mechanical, electronic, and thermal properties of $YNbNi_2Si_2$ and $YNbNi_2Ge_2$ double half-Heusler alloys. The Kohn–Sham equations were solved using the Projector Augmented-Wave (PAW) method, which tends to accurately describes the interaction between the atomic cores and valence electrons. For the PAW method, the all-electron wavefunction is reconstructed from a smooth pseudo-wavefunction using linear transformation operators [22]. This allows the inclusion of the full nodal character of valence wavefunctions near the nucleus without explicitly treating all core electrons, therefore combining the computational efficiency of pseudopotential methods with the accuracy of all-electron approaches. The PAW formalism expands the pseudo-wavefunction in a plane-wave basis set, while core–valence interactions are represented through augmentation spheres centered on each atom. This method provides improved precision in calculating total energies, forces, and electronic properties and is widely used in Quantum ESPRESSO and similar DFT codes [22,23]. In this work, PAW pseudopotentials were employed alongside Perdew–Burke–Ernzerhof (PBE) generalized gradient approximation (GGA) [24] since the combination offer a reliable balance between accuracy and computational cost. Initially, the $YNbNi_2Si_2$ and $YNbNi_2Ge_2$ structures underwent relaxation, ensuring that the energy and internal forces were minimized until they reached convergence thresholds. When the difference in total crystal energy remained less than 1.0×10^{-5}eV/atom, the self-consistent calculations were judged complete. The geometry was adjusted during the relaxation process until the ionic force was less than 0.03 eV/Å, the maximum ionic displacement was 0.001 Å, and the maximum stress was less than 0.05 GPa. The Monkhorst–Pack special k-point scheme [25] 10 × 5 × 7 k-points in the Brillouin zone were applied while dense k-points 20 × 10 × 14 were employed in computing the electronic properties. The cutoff energy for wave functions was set at 60 Ry and ecutrho at 480 Ry to ensure convergence was achieved.

Structural properties of $YNbNi_2Si_2$ and $YNbNi_2Ge_2$ alloys obtained using Murnaghan equation of states (see Fig. 2) below [26].

$$E(V) = E(V_0) + \frac{B_0 V}{B_0'(B_0'-1)}\left[V\left(\frac{V_0}{V}\right)^{1-B_0'} - 1\right] \tag{1}$$

One important property for evaluating a material's thermodynamic stability is its formation energy. The general formula is given by Eq. (2);[27].

$$\Delta H_f = E_{\text{tot}}^{\text{Material}} - \sum_i [n_i \mu_i] \tag{2}$$

Where the compound's formation energy (in eV/atom) is represented by ΔH_f, the total ground state energy of the compound is indicated $E_{\text{tot}}^{\text{bulk}}$. The number of atoms of element i in the compound is represented by n_i and μ_i. Eqs. (3)–(4) indicates how the formation energies of $YNbNi_2Si_2$ and $YNbNi_2Ge_2$ were calculated respectively.

$$\Delta H_f^{YNbNi_2Si_2} = E_{\text{tot}}^{YNbNi_2Si_2} - \left[\mu_Y + \mu_{Nb} + 2\mu_{Ni} + 2\mu_{Si}\right] \tag{3}$$

$$\Delta H_f^{YNbNi_2Ge_2} = E_{\text{tot}}^{YNbNi_2Ge_2} - \left[\mu_Y + \mu_{Nb} + 2\mu_{Ni} + 2\mu_{Ge}\right] \tag{4}$$

To obtain insight into mechanical properties, bulk modulus (B), shear modulus (G), Young's modulus (E), and Poisson's ratio (n) for $YNbNi_2Si_2$ and $YNbNi_2Ge_2$, calculated using Voigt–Reuss–Hill approximations [28].

$$B = \frac{B_V + B_R}{2} \tag{5}$$

$$G = \frac{G_V + G_R}{2} \tag{6}$$

$$E = \frac{9GB}{3B+G} \tag{7}$$

$$\nu = \frac{3B-2G}{6B+2G} \tag{8}$$

These mechanical parameters shed light on the alloys' resistance to deformation under various forms of stress and overall structural stability [29]

As one of the properties that determines microcrack induction, the analysis of elastic anisotropy is crucial to understanding the ductility of materials [30]. For instance the shear anisotropic ratio for the {100} shear planes between the {011} and {010} directions is expressed as;

$$A_{100} = \frac{4C_{44}}{C_{11}+C_{33}-2C_{13}} \tag{9}$$

while the {010} shear planes between {101} and {001} directions;

$$A_{010} = \frac{4C_{55}}{C_{22}+C_{33}-2C_{23}} \tag{10}$$

and that of the {001} shear planes between {110} and {110} directions given by;

$$A_{001} = \frac{4C_{66}}{C_{11}+C_{22}-2C_{12}} \tag{11}$$

The semiclassical Boltzmann transport equation was utilized to calculate thermoelectric transport coefficients scaled by relaxation time [31,32]. Since, the lattice thermal conductivity is not computed, the stated ZT values must be regarded as approximated upper limits.

3. Results and discussions

3.1. Structural properties

$YNbNi_2Si_2$ and $YNbNi_2Ge_2$ double half-Heusler alloys crystallize in simple orthorhombic system with space group Pmn_21 number 31 (see Fig. 1). Table 1 shows the structural properties of $YNbNi_2Si_2$ and $YNbNi_2Ge_2$ alloys as computed in this work. $YNbNi_2Ge_2$ (a = 4.158 Å) has a slightly greater lattice parameter than $YNbNi_2Si_2$ (a = 4.082 Å). This is predicted given that Ge atoms are bigger than Si atoms, resulting in an increase in total lattice size. Increased interatomic spacing can affect bond strength and phonon interactions, which are important for mechanical and thermoelectric properties. The b/a and c/a ratios are largely constant, with small deviations. This implies that the crystal structure is intact, with merely a uniform expansion occurring when Si

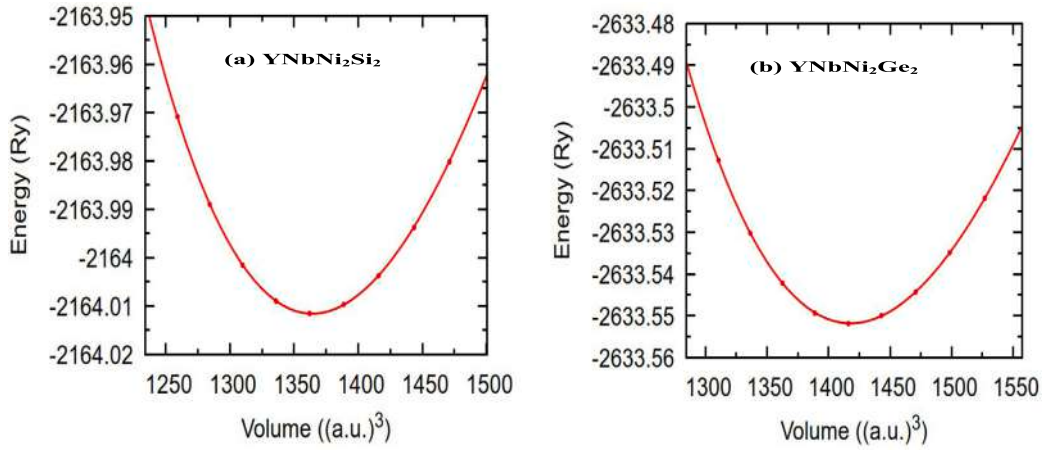

Fig. 2. Energy-volume curves of $YNbNi_2Si_2$ and $YNbNi_2Ge_2$ double half-Heusler alloys.

Table 1
Lattice constants a (Å), b/a, c/a, bulk modulus (B), partial derivative of B_0, volume V (Å^3), density ρ (g/cm^3) and formation energies of $YNbNi_2X_2$ (X = Si or Ge) double half Heusler alloys computed at ground state.

Alloy	a	b/a	c/a	B_0	B'_0	V	ρ	ΔH_f
$YNbNi_2Si_2$	4.082	2.060	1.440	127.05	4.513	16.82	5.846	−0.660
Others [20,21]								−0.774
$YNbNi_2Ge_2$	4.158	2.035	1.433	120.79	4.685	17.48	7.035	−0.630
Others [20,21]								−0.657

is replaced with Ge. $YNbNi_2Si_2$ has a higher bulk modulus (127.05 GPa) than $YNbNi_2Ge_2$ (120.79 GPa), showing mechanical stiffness and less compressibility. The softer lattice of $YNbNi_2Ge_2$ may increase phonon scattering while decreasing thermal conductivity. Both materials behave similarly to high-pressure environments, as seen by their identical B'_0 values (≈4.5). A modest increase in B'_0 for $YNbNi_2Ge_2$ (4.685 vs. 4.513) indicates a slower rate of stiffness reduction with pressure. The equilibrium volume of $YNbNi_2Ge_2$ (17.48 Å^3/atom) exceeds that of $YNbNi_2Si_2$(16.82 Å^3/atom). This continues the trend of larger atomic sizes from Si to Ge. A higher volume may result in longer bond lengths, reducing bonding strength and perhaps lowering mechanical stability. $YNbNi_2Ge_2$ is denser (7.035 g/cm^3) compared to $YNbNi_2Si_2$ (5.846 g/cm^3). This is due to Ge's greater atomic mass (72.63 u) compared to Si (28.09 u). Higher density can impact phonon scattering, which affects thermal conductivity and mechanical properties.

3.2. Formation energy

The formation energies of $YNbNi_2Ge_2$ and $YNbNi_2Ge_2$ were determined using DFT are −0.660 eV/atom and −0.630 eV/atom, respectively shown in Table 1. The negative values show that both materials are thermodynamically stable in relation to their constituent constituents. Furthermore, These formation energies suggest that both materials can potentially be synthesized experimentally and might exist in stable phases Additionally, $YNbNi_2Ge_2$ has a somewhat lower formation energy than $YNbNi_2Si_2$, indicating a slightly higher stability for $YNbNi_2Si_2$ alloy.

3.3. Mechanical properties

3.3.1. Elastic constants

Table 2 displays the elastic constants (C_{ij}) for the double half Heusler alloys $YNbNi_2Si_2$ and $YNbNi_2Ge_2$, indicating mechanical stability, stiffness, and resistance to deformation. The estimated values meet the Born stability criterion for orthorhombic crystals (equation 5–9) [33,34], indicating that both materials are mechanically stable while in equilibrium.

$$C_{11} > 0, C_{22} > 0, C_{44} > 0, C_{55} > 0, C_{66} > 0, \quad (12)$$

$$[C_{11} + C_{22} + C_{33} + 2(C_{12} + C_{13} + C_{23})] > 0, \quad (13)$$

$$(C_{11} + C_{22} - 2C_{12}) > 0, \quad (14)$$

$$(C_{11} + C_{33} - 2C_{12}) > 0, \quad (15)$$

$$(C_{22} + C_{33} - 2C_{23}) > 0. \quad (16)$$

The longitudinal elastic constants C_{11}, C_{22}, and C_{33} represent the resistance to uniaxial strain in distinct crystallographic orientations [35]. $YNbNi_2Si_2$ has somewhat higher values for C_{11} (239.02 GPa) and C_{33} (232.66 GPa) than $YNbNi_2Ge_2$ (225.39 GPa and 216.82 GPa, respectively). $YNbNi_2Si_2$ exhibits stronger atomic bonding and a stiffer lattice structure, making it more resistant to elastic deformation from external pressures. The elastic constants C_{44}, C_{55}, and C_{66} indicate the material's resistance to shape distortion. $YNbNi_2Si_2$ has slightly larger shear modulus values than $YNbNi_2Ge_2$, especially for C_{66} (77.93 GPa vs. 71.94 GPa), suggesting improved mechanical stiffness and resistance to shear strain. $YNbNi_2Ge_2$ has lower interplanar stiffness constants C_{12}, C_{13}, and C_{23} than $YNbNi_2Si_2$, indicating higher flexibility in the Ge-based compound. Reduced stiffness in $YNbNi_2Ge_2$ can improve phonon scattering, reducing lattice thermal conductivity, which is crucial for thermoelectric applications.

Table 3 presents the bulk modulus, Young's modulus, shear modulus and Poisson's ratio for the two alloys. $YNbNi_2Si_2$ has a slightly greater bulk modulus (B) (127.79 GPa) than $YNbNi_2Ge_2$ (121.70 GPa), which indicates a material's ability to withstand uniform compression. This suggests that $YNbNi_2Si_2$ has stronger interatomic bonds and is less compressible than $YNbNi_2Ge_2$. A greater bulk modulus indicates that the Si-based alloy has a denser, stiffer lattice structure. $YNbNi_2Si_2$ has a slightly higher shear modulus (67.44 GPa) than $YNbNi_2Ge_2$ (66.85 GPa), indicating its resistance to shape deformation under shear stress. $YNbNi_2Si_2$ exhibits higher stiffness and resistance to shear deformation, contributing to mechanical strength. The Young's modulus (E), which quantifies the stiffness of a material under uniaxial stress, follows a similar pattern. $YNbNi_2Si_2$ has a Young's modulus of 169.83 GPa while

Table 2
Elastic constants of $YNbNi_2Si_2$ and $YNbNi_2Ge_2$ double half-Heusler alloys in GPa.

	C_{11}	C_{22}	C_{33}	C_{44}	C_{55}	C_{66}	C_{12}	C_{13}	C_{23}
$YNbNi_2Si_2$	239.02	195.09	232.66	50.03	73.05	77.93	87.29	81.97	73.97
$YNbNi_2Ge_2$	225.39	195.00	216.82	56.25	72.02	71.94	79.98	78.08	71.74

Table 3
Bulk modulus (B), shear modulus (G), Young's modulus (E), and Poisson's ratio (n) of $YNbNi_2x_2$ (x=Si or Ge) as computed by GGA functionals.

Alloy	Bulk modulus (GPa)			Young's modulus (GPa)			Shear modulus (GPa)			Poisson's ratio		
	B_V	B_R	B	E_V	E_R	E	G_V	G_R	G	n_V	n_R	n
$YNbNi_2Si_2$	128.14	127.45	127.79	174.29	169.83	172.06	68.44	66.45	67.44	0.2733	0.2779	0.2755
$YNbNi_2Ge_2$	121.87	121.53	121.70	170.13	168.75	169.53	67.20	66.51	66.85	0.2670	0.2685	0.2678

Table 4
Cauchy's pressure of $YNbNi_2Si_2$ and $YNbNi_2Ge_2$ double half-Heusler Alloys.

	$YNbNi_2Si_2$	$YNbNi_2Ge_2$
P_x^{Cauchy}	23.94	15.49
P_y^{Cauchy}	8.92	6.06
P_z^{Cauchy}	9.36	8.04

$YNbNi_2Ge_2$has a slightly lower value of 168.75 GPa. These data show that $YNbNi_2Si_2$ is the stiffer material, despite the slight difference. Poisson's ratio (n) offers information on the material's ductility and the type of atomic bonding. $YNbNi_2Si_2$ has a Poisson's ratio (n) of 0.2755, and $YNbNi_2Ge_2$ has a slightly lower value of 0.2678. In general, a Poisson's ratio (n) less than 0.26 suggests brittleness, whereas values near 0.26 imply moderate ductility [36]. Both materials have slightly larger Poisson's ratios (n) than 0.26, suggesting that they are ductile rather than brittle. $YNbNi_2Si_2$ has larger bulk, shear, and Young's moduli than $YNbNi_2Ge_2$, resulting in greater mechanical stiffness and resistance to compression and shear deformation. $YNbNi_2Ge_2$ is more flexible, perhaps leading to improved phonon scattering and reduced thermal conductivity. This makes it a promising contender for thermoelectric applications. The comparatively low Poisson's ratios (n) of these compounds indicate restricted ductility, which reinforces their mechanical stiffness. Furthermore, based on the B and G, calculated values of Pugh's ratio (B/G) for $YNbNi_2Si_2$ (1.89) and $YNbNi_2Ge_2$ (1.82) were found to exceed the critical value 1.75 [37,38] confirming the ductile nature of the alloys.

In orthorhombic compounds, we define the Cauchy's pressure in x, y and z directions as indicated in Table 4. The Cauchy's pressure provides details on the bonding type as well as the ductile nature of a material. If the value of the Cauchy's pressure is positive, this implies that the material is ductile with metallic bonds. On the other hand, if its value is negative, the material is be brittle with directional covalent bonds. The ionic crystals have a large Cauchy's pressure either positive or negative [39]. $YNbNi_2Si_2$ and $YNbNi_2Ge_2$ Alloys have positive Cauchy's pressure in x-, y- and z-axes suggesting that the alloys are ductile in nature considering the three directions.

3.3.2. Elastic anisotropy

Table 5 presents the shear anisotropy factors A_{100}, A_{010}, and A_{001}, percent anisotropy factors for bulk (A_B) and shear (A_G) moduli, universal anisotropy factor (A^U), Vickers hardness (H_v), and melting temperature (T_m) of $YNbNi_2Si_2$ and $YNbNi_2Ge_2$. These parameters are essential for understanding the mechanical behavior, hardness, and thermal stability of these double half-Heusler alloys. Shear anisotropy factors A_{100}, A_{010}, and A_{001} show directional dependence of mechanical properties. A number around 1 indicates isotropic behavior, whereas deviations imply mechanical anisotropy. Both materials have anisotropy factors that depart from one, indicating some degree of anisotropy. However, $YNbNi_2Si_2$ has lower values, indicating that it is more isotropic than $YNbNi_2Ge_2$.

In addition to shear anisotropy, anisotropy of the linear bulk modulus is the source of elastic anisotropy of orthorhombic structures [40]. The following is an expression for the anisotropic ratios of the bulk modulus along the a- and c-axes with regard to the b-axis:

$$A_B = \frac{B_V - B_R}{B_V + B_R} \tag{17}$$

and

$$A_G = \frac{G_V - G_R}{G_V + G_R} \tag{18}$$

where B_V and G_V are the bulk and shear modulus from Voigt approximation while B_R and G_R are bulk and shear modulus from Reuss approximation, respectively. The crystal exhibits the maximum elastic anisotropy when A_B=A_G=1, but it is elastically isotropic when A_B=A_G=0. The percent anisotropy factors (A_B and A_G) show that $YNbNi_2Ge_2$ has somewhat lower anisotropy in bulk and shear moduli than $YNbNi_2Si_2$. We determined the universal anisotropic index given by Eq. (19) to get a better understanding of the anisotropic the features of the $YNbNi_2Si_2$ and $YNbNi_2Ge_2$ structures using equation 16 [41].

$$A^U = 5(\frac{G_V}{G_R}) + \frac{B_V}{B_R} - 6 \tag{19}$$

where B_V and G_V are the bulk and shear modulus from Voigt approximation while B_R and G_R are bulk and shear modulus from Reuss approximation, respectively. The elastic anisotropy index (AU) of the elastically isotropic crystals must be zero; otherwise, the crystals are anisotropic. $YNbNi_2Si_2$ has a larger AU A^U (0.1551) than $YNbNi_2Ge_2$ (0.0470), suggesting a more anisotropic material.

$YNbNi_2Si_2$ has larger anisotropy, higher melting temperature, and somewhat lower hardness than $YNbNi_2Ge_2$. The Ge-based composite is somewhat tougher, but less anisotropic and has a lower melting point. These qualities indicate that $YNbNi_2Si_2$ is better appropriate for applications needing high thermal stability, whereas $YNbNi_2Ge_2$ may be favorable in cases where hardness is a vital feature.

3.3.3. Vickers hardness

A material's hardness describes its elasticity or plasticity. In this work, Chen's model [42,43] was used to estimate the Vickers hardness (H_v) of materials in the study since it yields findings that are significantly closer to the experiment. Vickers hardness of a material is given by an expression;

$$H_v = 2(\frac{G^3}{B^2})^{0.585} - 3 \tag{20}$$

where B and G are Bulk modulus and shear modulus respectively. $YNbNi_2Ge_2$ has a slightly greater Vickers hardness (H_v) (8.595 GPa) than $YNbNi_2Si_2$ (8.121 GPa), indicating its resistance to indentation. This shows that the Ge-based compound is somewhat tougher.

3.3.4. Melting point

The melting point of intermetallic alloys can be approximately from their elastic constants because stronger bonds and greater thermal stability are typically associated with stiffer alloys (bulk modulus, shear

Table 5
The shear anisotropy factors ($A_{\{100\}}, A_{\{010\}}, A_{\{001\}}$), percent anisotropy factors of bulk (A_B)and shear (A_G) moduli, universal anisotropy factor A^U, and Vickers hardness (H_v) in GPa for $YNbNi_2Si_2$ and $YNbNi_2Ge_2$ alloys.

Alloy	$A_{\{100\}}$	$A_{\{010\}}$	$A_{\{001\}}$	A_B	A_G	A^U	H_v	T_m
$YNbNi_2Si_2$	0.650	1.04	1.201	0.0028	0.0147	0.1551	8.121	1420
$YNbNi_2Ge_2$	0.796	1.07	1.089	0.0013	0.0051	0.0470	8.595	1355

modulus, or elastic constants). A number of semi-empirical models have been put forth to relate elastic constants to melting point (T_m). An empirical correlation that is frequently used for orthorhombic systems is based on the elastic constant C_{11} and C_{33}. The melting points of the $YNbNi_2Si_2$ and $YNbNi_2Ge_2$ alloys were predicted by replacing C_{11} and C_{33} in Eq. (21) [44,45].

$$T_m = 354 + 4.5(2C_{11} + C_{33})/3 \quad (21)$$

$YNbNi_2Si_2$ has a higher melting point (1420 K) than $YNbNi_2Ge_2$ (1355 K), indicating improved thermal stability in high-temperature applications.

3.4. Electronic properties

3.4.1. Electronic band structure

With indirect band gaps of 0.51 eV and 0.56 eV, respectively, the electrical band structures of $YNbNi_2Si_2$ and $YNbNi_2Ge_2$, as shown in Fig. 3, demonstrate their semiconducting character. In comparison to $YNbNi_2Si_2$ (0.51 eV), $YNbNi_2Ge_2$ has a slightly higher band gap (0.56 eV), indicating that it may have a smaller intrinsic carrier concentration at ambient temperature, which might impact its electrical conductivity. Both alloys exhibit discernible dispersion in their valence and conduction bands, suggesting comparatively low effective masses for charge carriers. This dispersion of the band suggests good carrier mobility, which is beneficial for thermoelectric performance [46]. Furthermore, the inclusion of Spin-Orbit Coupling (SOC) in the calculations for both $YNbNi_2Si_2$ and $YNbNi_2Ge_2$ leads to significant modifications in their electronic band structures, primarily characterized by band splitting of energy levels. Valence bands moved away from the fermi level while conduction band moved towards the Fermi level with SOC calculations, altering the electronic properties. These findings are critical for a precise understanding of the materials' electronic properties.

3.4.2. Partial and total density of states

The Fig. 4 presents the total and projected density of states (PDOS) for $YNbNi_2Si_2$ and $YNbNi_2Ge_2$ double half-Heusler alloys. Fig. 4: (a) and (b) display the total density of states (DOS) for $YNbNi_2Si_2$ and $YNbNi_2Ge_2$, respectively, revealing the overall electronic structure and indicating the presence of a band gap. The PDOS plots for the constituent elements further elucidate the contributions of different atomic orbitals to the electronic states. Fig. 4: (c) and (d) illustrate the PDOS for yttrium (Y) in both compounds, showing dominant contributions from Y-d orbitals around the Fermi level. Similarly, Fig. 4: (e) and (f) depict the PDOS of niobium (Nb), where the Nb-d states play a significant role in electronic behavior. The PDOS of nickel (Ni) in Fig. 4: (g) and (h) highlights a major contribution from Ni-d orbitals, which significantly shape the valence and conduction bands. Finally, Fig. 4: (i) and (j) compare the contributions of silicon (Si) and germanium (Ge), where the Si-p and Ge-p orbitals influence the electronic states near the band edges. Overall, the analysis provides insights into the electronic structure and bonding characteristics of these double half-Heusler alloys. The projected density of states (PDOS) analysis highlights the dominant orbital contributions near the Fermi level, with Y-d, Nb-d, and Ni-d states playing a crucial role in electronic transport. The strong hybridization between transition metal d-states and main group p-states suggests the possibility of low lattice thermal conductivity due to enhanced phonon scattering. This is beneficial for achieving high thermoelectric efficiency, as it helps maintain a high figure of merit (ZT) by reducing thermal conductivity. These insights provide a foundation for optimizing these double half-Heusler alloys for energy conversion applications by tailoring electronic and thermal transport properties.

3.5. Thermal properties

From Fig. 5(a), it is evident that at low temperatures (T< 100K) debye vibrational energies in both cases are reduced, resulting in fewer phonons being stimulated. This leads to a greater mean free path and thermal conductivity. The vibrational energy increases substantially with temperature, resulting in increased phonon–phonon scattering. This decreases the phonon mean free path and lowers lattice thermal conductivities. At high temperatures (T> 400K), debye vibrational energy follows a linear trend, indicating that phonon scattering has saturated and lattice thermal conductivities have reached its lowest. Since $YNbNi_2Ge_2$ has slightly lower vibrational energy, it is likely to have lower lattice thermal conductivity, making it a better thermoelectric material than $YNbNi_2Si_2$.

Both materials show a decrease in Debye vibrational free energy as temperature increases as demonstrated in Fig. 5(b). This tendency is consistent with the predicted thermodynamic behavior, in which vibrational free energy falls as thermal energy increases. At any temperature, $YNbNi_2Si_2$ has more vibrational free energy than $YNbNi_2Ge_2$. This shows that $YNbNi_2Si_2$. preserves slightly more vibrational energy than $YNbNi_2Ge_2$. at the same temperature. In both materials, the Debye entropy increases with temperature as clearly observed in Fig. 5(c). At low temperatures (T < 100 K), entropy is minimal, but rapidly increases as temperature increases. At higher temperatures (T > 600 K), entropy increases at a slower rate. The Debye entropy is proportional to the phonon (lattice vibration) contributions to the system's thermodynamics. $YNbNi_2Ge_2$ has more entropy than $YNbNi_2Si_2$ because to the softer (lower frequency) vibrational modes caused by Ge's heavier nature. This means that $YNbNi_2Ge_2$ has more readily available microstates, resulting in its greater entropy.

At high temperatures, C_V approaches a constant value (approximately 3R per mole of atoms), as per the conventional Dulong-Petit law [47]. Because both materials converge to the same value as shown in Fig. 5(d), they exhibit standard thermodynamic behavior. Higher heat capacity indicates that the material can absorb more heat per unit temperature change. $YNbNi_2Ge_2$ may exhibit superior thermal stability and expansion than $YNbNi_2Si_2$ due to its somewhat larger heat capacity. This might be useful in high-temperature applications like thermoelectrics and superconducting materials, where thermal management is critical.

3.6. Thermoelectric properties

Assuming the relaxation time constant, the Boltztrap2 package (based on semi-classical theory) which utilizes the electronic band structure to compute transport coefficients calculated using first-principles methods [31,32] . Constant chemical potentials, 0.8480 Ry and 0.8764 Ry equivalent to Fermi level of $YNbNi_2Si_2$ and $YNbNi_2Ge_2$ respectively were used to calculate the thermoelectric properties. The Fermi level in an intrinsic semiconductor at equilibrium is the chemical potential of electrons; it controls carrier concentrations and is fixed by the requirement of overall charge neutrality, [48,49]. The calculated TE parameters plotted against temperature (300–1000 K), which is approximately within the theoretically predicted melting points in Section 3.2.

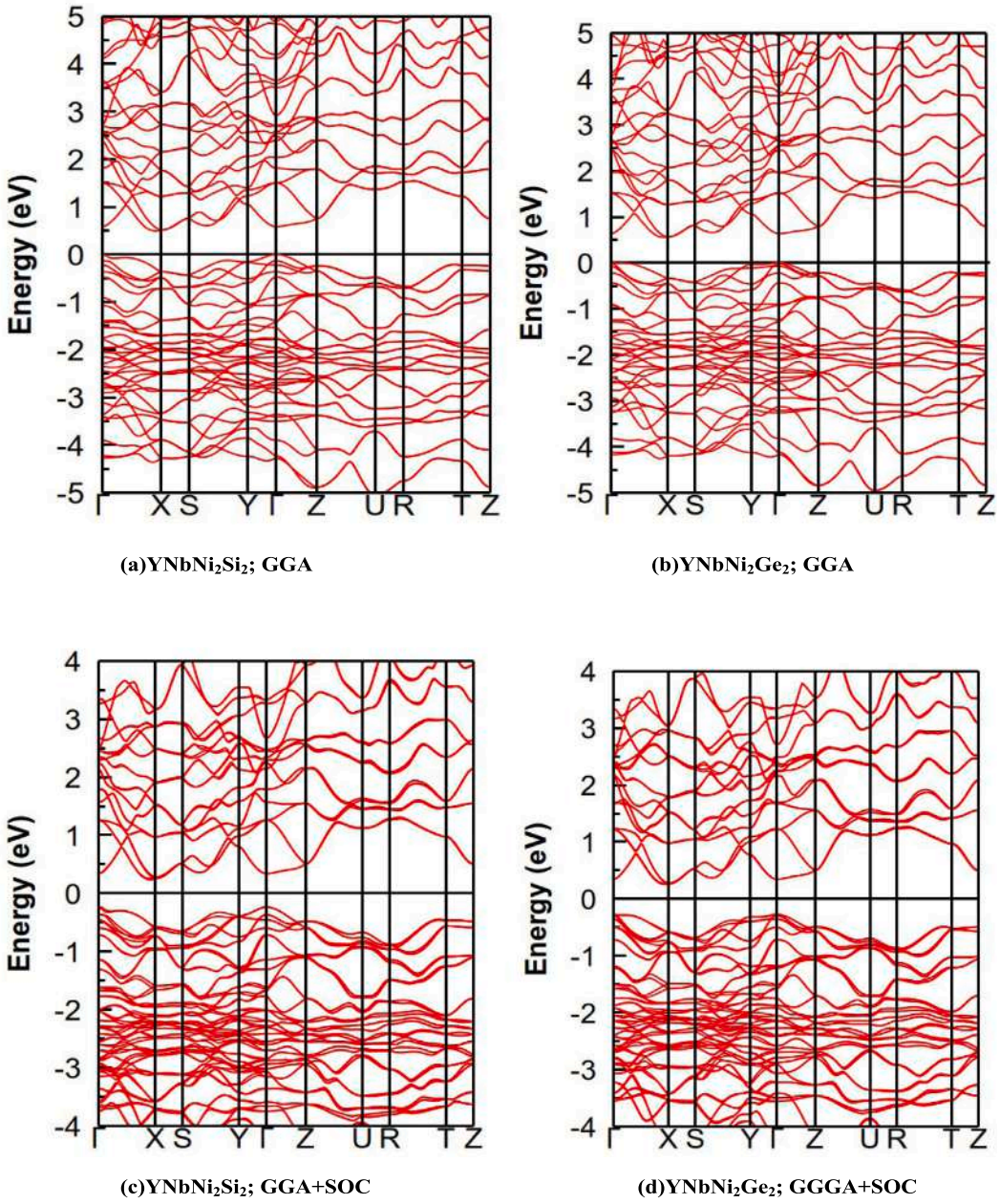

Fig. 3. Electronic band structures for $YNbNi_2Si_2$ and $YNbNi_2Ge_2$ double half-Heusler alloys, comparing calculations performed using the Generalized Gradient Approximation (GGA) both with and without the inclusion of Spin-Orbit Coupling (SOC). The plots illustrate energy levels relative to the Fermi level (0 eV) along high-symmetry k-points.

3.6.1. Electrical conductivity (σ)

The electrical conductivity measures the number of electrons/holes in the conduction band as well a measure of the flow of electronic charge in a material [50,51]. Fig. 6: (a) shows the temperature dependence of electrical conductivity (σ) in $YNbNi_2Si_2$ and $YNbNi_2Ge_2$ double half-Heusler alloys. Both alloys' electrical conductivity rises with temperature across the tested range (300-1000 K), indicating semiconducting nature. This pattern shows that thermal excitation causes a rise in charge carrier concentration, which improves conductivity at high temperatures. A comparison of the two materials demonstrates that $YNbNi_2Si_2$ displays consistently greater electrical conductivity than $YNbNi_2Ge_2$, indicating that $YNbNi_2Si_2$ likely has a higher intrinsic carrier concentration or superior charge transport properties. The observed conductivity behavior has a substantial impact on thermoelectric performance. Higher electrical conductivity improves the power factor (σS^2), which directly affects the efficiency of thermoelectric energy conversion. Optimizing the balance between electrical conductivity and the Seebeck coefficient is critical, since increasing σ can occasionally lead to a drop in S, hence restricting the total thermoelectric figure of merit (ZT).

3.6.2. Thermal conductivity

Fig. 6: (b) depicts the electronic thermal conductivity (k_e) as a function of temperature for $YNbNi_2Si_2$ and $YNbNi_2Ge_2$ double half-Heusler alloys. Both materials' electronic thermal conductivity rises with temperature, following a nearly linear pattern. This trend is predicted, as electronic thermal conductivity is closely connected to electrical conductivity via the Wiedemann–Franz rule ($k_e = L\sigma T$), where L is the Lorenz number [52]. Electrical conductivity (σ) rises with temperature, therefore the increase in k_e is consistent with this

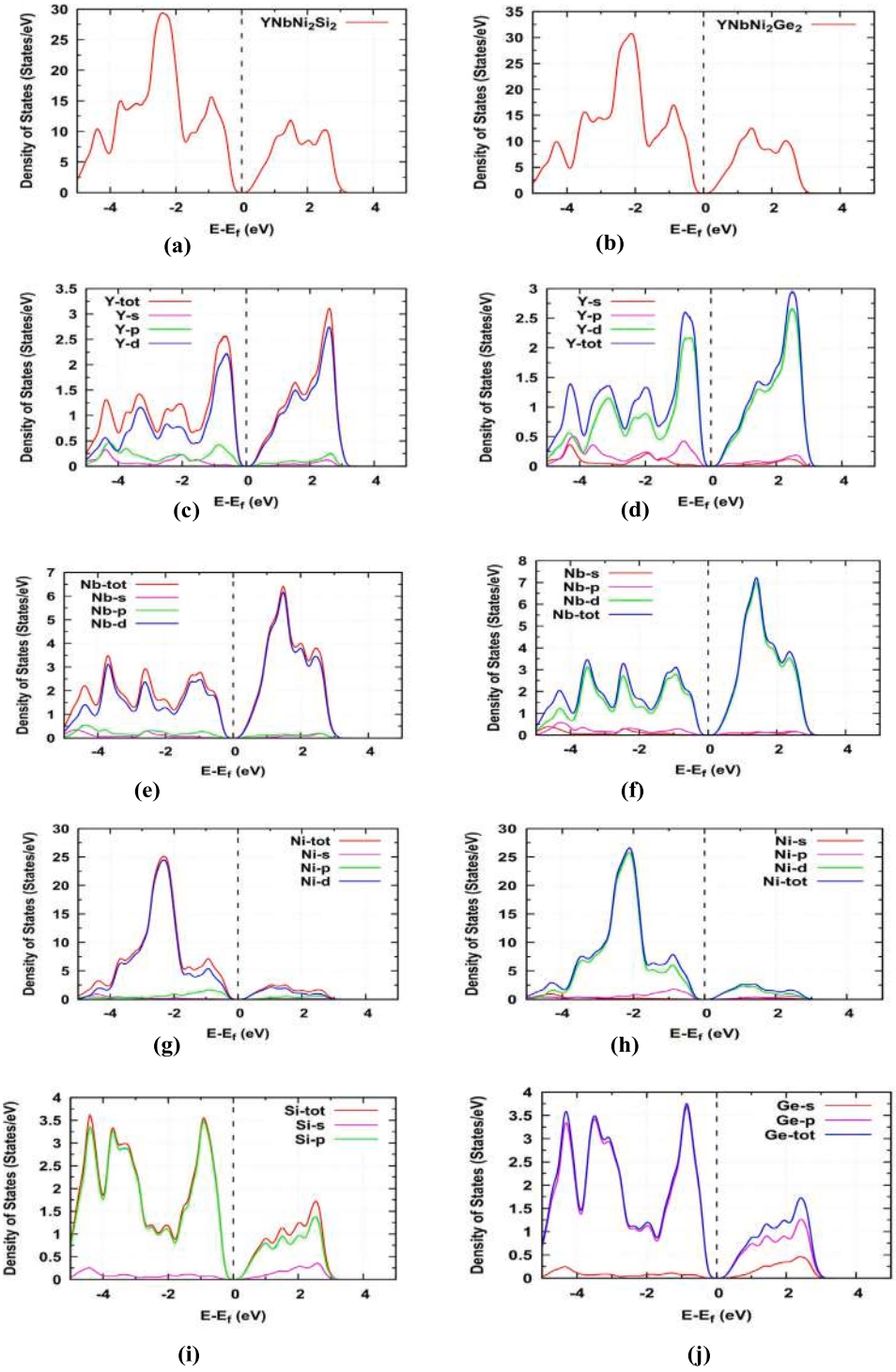

Fig. 4. PDOS and total DOS of $YNbNi_2Si_2$ and $YNbNi_2Ge_2$ double half-Heusler alloys.

connection. Comparing the two materials, $YNbNi_2Si_2$ has somewhat greater electronic thermal conductivity than $YNbNi_2Ge_2$. This difference is consistent with the observed increase in electrical conductivity, since higher carrier mobility and concentration in $YNbNi_2Si_2$ contribute to greater heat transfer via charge carriers. However, in thermoelectric applications, lower thermal conductivity is often preferred in order to maintain a high temperature gradient and increase efficiency. Because total thermal conductivity (k) is the sum of electronic (k_e) and lattice (k_l) thermal conductivity, an increase in k_e may negatively effect the figure of merit (ZT).

3.6.3. Seebeck coefficient (S)

The temperature dependence of the Seebeck coefficient (S) for p-type $YNbNi_2Si_2$ and p-type $YNbNi_2Ge_2$ thermoelectric materials is depicted in Fig. 6: (c). For both materials, the Seebeck coefficient increases with temperature, eventually reaching saturation. This is the

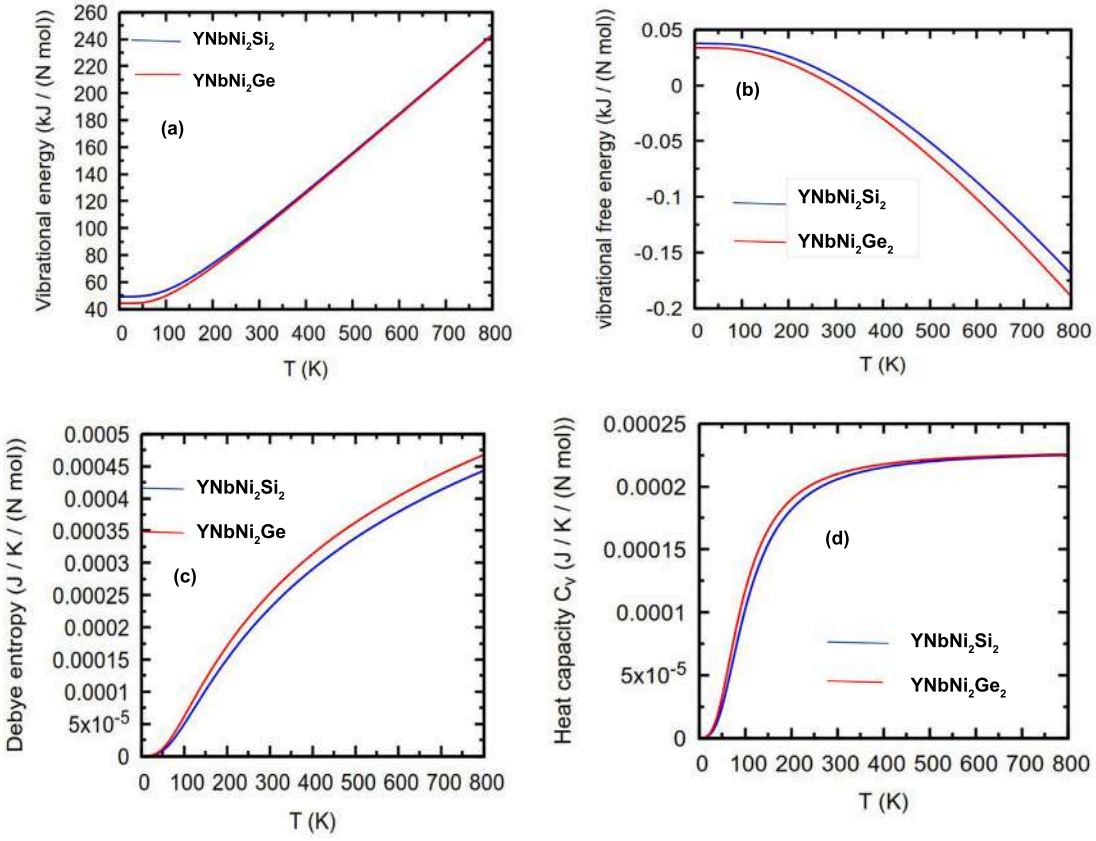

Fig. 5. Thermal properties of $YNbNi_2Si_2$ and $YNbNi_2Ge_2$ double half-Heusler alloys as a function of temperature.

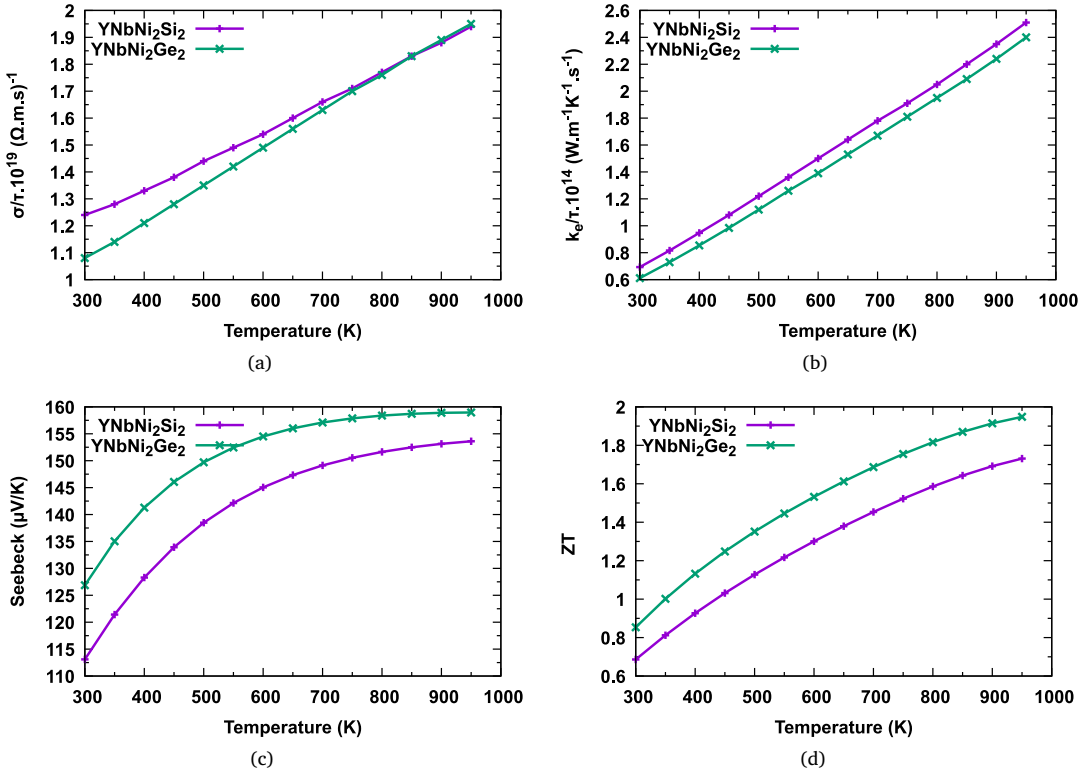

Fig. 6. Temperature dependent thermoelectric properties of $YNbNi_2Si_2$ and $YNbNi_2Ge_2$ double half-Heusler alloys.

property of thermoelectric semiconductors, where increasing temperature improves carrier excitation, resulting in increased thermoelectric voltage production. The saturation of (S) at temperatures above 700 K, point to a limit to the increases in carrier mobility [53]. When comparing the two compounds, $YNbNi_2Ge_2$ has a larger Seebeck coefficient than $YNbNi_2Si_2$ over the temperature range. This implies that $YNbNi_2Ge_2$ has lower carrier concentration or a more favorable band structure for thermoelectric power production. Materials with lower charge carrier density have higher Seebeck coefficients, according to the equation $S \propto \frac{1}{n}$ (where n is the carrier concentration) [54]. Maintaining an appropriate balance between S and electrical conductivity (σ) is critical for improving the power factor $PF = \sigma S^2$. A higher Seebeck coefficient improves thermoelectric performance because it leads to a larger thermoelectric voltage per unit temperature difference [55]. Because the thermoelectric figure of merit (ZT) is directly proportional to S^2, the higher Seebeck coefficient of $YNbNi_2Ge_2$ suggests its potential for better thermoelectric efficiency than $YNbNi_2Si_2$, provided that electrical and thermal conductivity are optimized.

3.6.4. Figure of merit (ZT)

The thermoelectric figure of merit (ZT) for $YNbNi_2Si_2$ and $YNbNi_2Ge_2$ double half-Heusler alloys varies with temperature, as shown in Fig. 6: (d). The ZT value for both materials increases with temperature, which is a common tendency in thermoelectric materials, as higher temperatures frequently boost electrical conductivity and the Seebeck coefficient while diminishing lattice thermal conductivity. $YNbNi_2Ge_2$ has a higher ZT than $YNbNi_2Si_2$ throughout the full temperature range, indicating a stronger thermoelectric potential. However, it is crucial to highlight that these findings are derived using the BoltzTraP algorithm, which does not account for lattice thermal conductivity (k_l). Neglecting k_l may result in an overestimation of ZT since the overall thermal conductivity (k) is the sum of electronic (k_e) and lattice (k_l) components. Thus, the values shown in Fig. 6: (d) should be interpreted as theoretical predictions and to achieve a more accurate estimate of ZT, phonon-related calculations, such as those done using Phono3py or ShengBTE code, are required to incorporate lattice thermal conductivity contributions. Nonetheless, the trends found in Fig. 6: (d) suggest that $YNbNi_2Ge_2$ has a larger potential for thermoelectric applications than $YNbNi_2Si_2$, as long as its lattice thermal conductivity remains low.

4. Conclusion

This work used density functional theory (DFT) computations to investigate the structural, mechanical, electrical, and thermoelectric characteristics of $YNbNi_2Si_2$ and $YNbNi_2Ge_2$ double half-Heusler alloys. The formation enthalpies from this study validate both alloys' thermodynamical stability, whereas the elastic constants meet the Born stability criterion, indicating their mechanical stability. Furthermore, the bulk modulus, shear modulus, and Poisson's ratio analyses indicate that both materials have ductile behavior, which is helpful for possible thermoelectric device applications. Electronic structure calculations show that $YNbNi_2Si_2$ and $YNbNi_2Ge_2$ are semiconductors, with direct band gaps of 0.512 eV and 0.5605 eV, respectively. The density of states (DOS) and band dispersion show strong hybridization between transition metal d-orbitals and main group element p-orbitals. This boosts carrier mobility, a key feature for high thermoelectric efficiency. The thermoelectric transport properties, calculated using the Boltzmann transport equation, demonstrate that $YNbNi_2Si_2$ displays better electrical conductivity, whereas $YNbNi_2Ge_2$ has superior Seebeck coefficient, suggesting distinct charge carrier dynamics. The figure of merit (ZT) rises with temperature for both materials. $YNbNi_2Ge_2$ has a higher anticipated ZT, making it the more attractive contender for thermoelectric applications. However, these calculations were done within the constant relaxation time approximation and did not explicitly consider lattice thermal conductivity (k_l), therefore, the anticipated ZT values should be taken as theoretical upper limits. More research into phonon interactions, anharmonic effects, and experimental validation is required to improve these predictions and achieve a more precise estimate of thermoelectric performance. Future research should look at doping, strain engineering, and nanostructuring techniques to improve carrier concentration and lower lattice thermal conductivity, thereby increasing total thermoelectric efficiency. Overall, the findings show that $YNbNi_2Si_2$ and $YNbNi_2Ge_2$ are feasible thermoelectric materials. Their potential structural stability, good electronic properties, and expected high thermoelectric performance indicate that these alloys might make a substantial contribution to the development of next-generation energy harvesting devices.

CRediT authorship contribution statement

Job W. Wafula: Writing – review & editing, Writing – original draft, Visualization, Validation, Software, Resources, Methodology, Investigation, Formal analysis, Conceptualization. **George S. Manyali:** Visualization, Validation, Supervision, Software, Project administration, Methodology, Investigation, Funding acquisition, Formal analysis, Data curation. **John W. Makokha:** Validation, Supervision, Software, Resources, Project administration, Methodology, Investigation, Formal analysis.

Declaration of competing interest

The authors declare that they have no known competing financial interests or personal relationships that could have appeared to influence the work reported in this paper.

Acknowledgments

First, the authors appreciate Kibabii University's Department of Science, Technology, and Engineering for providing platform as well as the internet services used to access the CHPC. Secondly, we recognize the Centre for High Performance Computing (CHPC) in Cape Town, South Africa, for their HPC resources. This work was also funded by the African Laser Center Research Grant No. HLHA25X task ALC-R015. Finally, we thank the Cambridge Crystallographic Data Centre for providing us with a license (Agreement Number: 021933/2024/1) to access the scientific information useful to this study.

Data availability

Data will be made available on request.

References

[1] M.Y. Khan, M.A. Jehangir, N. Israr, A. Hassan, U. Younis, J. Khan, M. Khan, A. Khan, A. Al Souwaileh, First-principles study of Cs3SbX6 (x=f, cl) for scintillation and optoelectronic applications, Phys. B 707 (2025) 417150.
[2] M. Ishfaq, S.A. Aldaghfag, M. Yaseen, U. Younis, R. Neffati, et al., First principles insight into physical properties of CaX2O4 (x=in, gd) spinels for optical and spintronic applications, J. Solid State Chem. 322 (2023) 123999.
[3] O. Caballero-Calero, J.R. Ares, M. Martín-González, Environmentally friendly thermoelectric materials: High performance from inorganic components with low toxicity and abundance in the earth, Adv. Sustain. Syst. 5 (11) (2021) 2100095.
[4] M. Martín-González, O. Caballero-Calero, Thermoelectric generators as an alternative for reliable powering of wearable devices with wasted heat, J. Solid State Chem. 316 (2022) 123543.
[5] D. Sarkar, A. Bhui, I. Maria, M. Dutta, K. Biswas, Hidden structures: a driving factor to achieve low thermal conductivity and high thermoelectric performance, Chem. Soc. Rev. (2024).
[6] L. Huang, Q. Zhang, B. Yuan, X. Lai, X. Yan, Z. Ren, Recent progress in half-Heusler thermoelectric materials, Mater. Res. Bull. 76 (2016) 107–112.
[7] Y. Rached, M. Caid, H. Rached, M. Merabet, S. Benalia, S. Al-Qaisi, L. Djoudi, D. Rached, Theoretical insight into the stability, magneto-electronic and thermoelectric properties of xcrsb (x: Fe, Ni) half-Heusler alloys and their superlattices, J. Supercond. Nov. Magn. 35 (3) (2022) 875–887.

[8] Z. Feng, Y. Fu, A. Putatunda, Y. Zhang, D.J. Singh, Electronic structure as a guide in screening for potential thermoelectrics: Demonstration for half-Heusler compounds, Phys. Rev. B 100 (8) (2019) 085202.

[9] H. Zhu, R. He, J. Mao, Q. Zhu, C. Li, J. Sun, W. Ren, Y. Wang, Z. Liu, Z. Tang, et al., Discovery of ZrCoBi based half Heuslers with high thermoelectric conversion efficiency, Nat. Commun. 9 (1) (2018) 2497.

[10] S. Erden Gulebaglan, E. Kilit Dogan, A comparison study of the structural electronic, elastic and lattice dynamic properties of ZrInAu and zrsnpt, Z. Für Naturforschung A 76 (6) (2021) 559–567.

[11] J.W. Wafula, Structural, elastic, electronic, optical and thermal properties of ymau (m=si or ge or sn) half-Heusler compounds; a DFT study, Results Mater. (2023) 100413.

[12] S. Guo, Z. Liu, Z. Feng, T. Jia, S. Anand, G.J. Snyder, Y. Zhang, Prediction of improved thermoelectric performance by ordering in double half-Heusler materials, J. Mater. Chem. A 8 (44) (2020) 23590–23598.

[13] S. Anand, M. Wood, Y. Xia, C. Wolverton, G.J. Snyder, Double half-heuslers, Joule 3 (5) (2019) 1226–1238.

[14] B. Sahni, A. Alam, Double half-Heusler alloys x 2 Ni 2 InSb (x=zr, hf) with promising thermoelectric performance: The role of varying structural phases, Phys. Rev. Appl. 22 (3) (2024) 034034.

[15] K. Zhang, Y. Zhang, S. Wang, Enhancing thermoelectric properties of organic composites through hierarchical nanostructures, Sci. Rep. 3 (1) (2013) 3448.

[16] S. Guo, T. Jia, Y. Zhang, Electrical property dominated promising half-Heusler thermoelectrics through high-throughput material computations, J. Phys. Chem. C 123 (31) (2019) 18824–18833.

[17] K. Xia, C. Hu, C. Fu, X. Zhao, T. Zhu, Half-Heusler thermoelectric materials, Appl. Phys. Lett. 118 (14) (2021).

[18] J. Yu, K. Xia, X. Zhao, T. Zhu, High performance p-type half-Heusler thermoelectric materials, J. Phys. D: Appl. Phys. 51 (11) (2018) 113001.

[19] P. Giannozzi, O. Andreussi, T. Brumme, O. Bunau, M.B. Nardelli, M. Calandra, R. Car, C. Cavazzoni, D. Ceresoli, M. Cococcioni, et al., Advanced capabilities for materials modelling with quantum ESPRESSO, J. Phys.: Condens. Matter. 29 (46) (2017) 465901.

[20] S. Kirklin, J.E. Saal, B. Meredig, A. Thompson, J.W. Doak, M. Aykol, S. Rühl, C. Wolverton, The open quantum materials database (OQMD): assessing the accuracy of DFT formation energies, Npj Comput. Mater. 1 (1) (2015) 1–15.

[21] J.E. Saal, S. Kirklin, M. Aykol, B. Meredig, C. Wolverton, Materials design and discovery with high-throughput density functional theory: the open quantum materials database (OQMD), Jom 65 (2013) 1501–1509.

[22] P.E. Blöchl, Projector augmented-wave method, Phys. Rev. B 50 (24) (1994) 17953.

[23] G. Kresse, D. Joubert, From ultrasoft pseudopotentials to the projector augmented-wave method, Phys. Rev. B 59 (3) (1999) 1758.

[24] J.P. Perdew, K. Burke, M. Ernzerhof, Generalized gradient approximation made simple, Phys. Rev. Lett. 77 (18) (1996) 3865.

[25] H.J. Monkhorst, J.D. Pack, Special points for brillouin-zone integrations, Phys. Rev. B 13 (12) (1976) 5188.

[26] F.D. Murnaghan, The compressibility of media under extreme pressures, Proc. Natl. Acad. Sci. 30 (9) (1944) 244–247.

[27] A.A. Emery, C. Wolverton, High-throughput DFT calculations of formation energy, stability and oxygen vacancy formation energy of ABO3 perovskites, Sci. Data 4 (1) (2017) 1–10.

[28] R. Hill, The elastic behaviour of a crystalline aggregate, Proc. Phys. Soc. Sect. A 65 (5) (1952) 349.

[29] R. Yang, M. Shi, Q. Wei, F. Wu, M. Xue, Y. Zhou, A first-principles study of the properties of P-43m-si3× 2 (x= n, p and as), Chinese J. Phys. 59 (2019) 535–545.

[30] V. Tvergaard, J.W. Hutchinson, Microcracking in ceramics induced by thermal expansion or elastic anisotropy, J. Am. Ceram. Soc. 71 (3) (1988) 157–166.

[31] G.K. Madsen, J. Carrete, M.J. Verstraete, BoltzTraP2, a program for interpolating band structures and calculating semi-classical transport coefficients, Comput. Phys. Comm. 231 (2018) 140–145.

[32] A. Kumar, N. Singh, A. Kumar, A. Garg, S.K. Pundir, N. Singh, Influence of mn doping on magneto-thermoelectric properties of spintronic material ZnMnxSn1-xAs2, Solid State Commun. (2025) 115971.

[33] Q. Fan, Q. Wei, H. Yan, M. Zhang, D. Zhang, J. Zhang, A new potential superhard phase of OsN_2, Acta Phys. Pol. A 126 (3) (2014) 740–746.

[34] J.W. Wafula, G.S. Manyali, J.W. Makokha, DFT calculations of elastic, electronic and thermal properties of tib2mo, Oxf. Open Mater. Sci. 2 (1) (2022) itac001.

[35] M. Radjai, D. Maouche, N. Guechi, S. Cheddadi, Z. Kechidi, Investigation of structural and elastic properties of monoclinic Ba _2 P _7 X (X = Cl, Br, I) Zintl Salts compounds, 2019, arXiv preprint arXiv:1910.00915.

[36] W.-C. Hu, Y. Liu, D.-J. Li, X.-Q. Zeng, C.-S. Xu, First-principles study of structural and electronic properties of C14-type laves phase Al2Zr and Al2Hf, Comput. Mater. Sci. 83 (2014) 27–34.

[37] K. Hussain, U. Younis, I. Muhammad, Y. Qie, Y. Guo, T. Li, H. Xie, Q. Sun, Three-dimensional porous borocarbonitride bc 2 n with negative Poisson's ratio, J. Mater. Chem. C 8 (44) (2020) 15771–15777.

[38] S. Pugh, XcII. Relations between the elastic moduli and the plastic properties of polycrystalline pure metals, Lond. Edinb. Dublin Philos. Mag. J. Sci. 45 (367) (1954) 823–843.

[39] S. Ahmad, R. Ahmad, S. Jalali-Asadabadi, Z. Ali, I. Ahmad, First principle studies of structural, magnetic and elastic properties of orthorhombic rare-earth diaurides intermetallics RAu2 (r=la, ce, pr and eu), Mater. Chem. Phys. 212 (2018) 44–50.

[40] F. Vahldiek, S. Mersol, Anisotropy in single crystal refractory compounds: Vols. 1 & 2, 1968.

[41] H. Ozisik, K. Colakoglu, E. Deligoz, First-principles study of structural and mechanical properties of agb2 and AuB2 compounds under pressure, Comput. Mater. Sci. 51 (1) (2012) 83–90.

[42] X.-Q. Chen, H. Niu, D. Li, Y. Li, Modeling hardness of polycrystalline materials and bulk metallic glasses, Intermetallics 19 (9) (2011) 1275–1281.

[43] J.W. Wafula, J.W. Makokha, G.S. Manyali, First-principles calculations to investigate structural, elastic, electronic and thermodynamic properties of NbCoSn and vrhsn half-Heusler compounds, Results Phys. 43 (2022) 106132.

[44] M. Fine, L. Brown, H. Marcus, Elastic constants versus melting temperature in metals, Scr. Metall. 18 (9) (1984) 951–956.

[45] X. Wang, M. Yan, H. Chen, et al., First-principle calculations of the hardness and melting point of Mo2C, J. Mater. Technol. 25 (03) (2009) 419.

[46] X. Zhou, Y. Yan, X. Lu, H. Zhu, X. Han, G. Chen, Z. Ren, Routes for high-performance thermoelectric materials, Mater. Today 21 (9) (2018) 974–988.

[47] P.L. Dulong, A.-T. Petit, Recherches sur quelques points importans de la theorie de la chaleur, 1819.

[48] F. Flores, R. Perez, R. Rincon, R. Saiz-Pardo, Electron states at semiconductor interfaces: the intrinsic and extrinsic charge neutrality levels, Philos. Trans. R. Soc. Lond. Ser. A: Phys. Eng. Sci. 344 (1673) (1993) 567–577.

[49] V. Brudnyi, Charge neutrality in semiconductors: defects, interfaces, surface, Russian Phys. J. 56 (7) (2013) 754–756.

[50] Q. Mahmood, T. Ghrib, A. Rached, A. Laref, M. Kamran, Probing of mechanical, optical and thermoelectric characteristics of double perovskites Cs2GeCl/Br6 by DFT method, Mater. Sci. Semicond. Process. 112 (2020) 105009.

[51] S. Berri, Thermoelectric properties of A2bcl6: a first principles study, J. Phys. Chem. Solids 170 (2022) 110940.

[52] S. Yigen, A. Champagne, Wiedemann–Franz relation and thermal-transistor effect in suspended graphene, Nano Lett. 14 (1) (2014) 289–293.

[53] N.K. Singh, A. Kumar, S. Kumar, V.K. Nautiyal, R. Kumar, A. Kumar, N. Iram, A comprehensive theoretical analysis of Cs2KGaX6 (x=cl, br, i): For green energy solutions, Solid State Commun. 401 (2025) 115929.

[54] K.H. Lee, S.-i. Kim, J.-C. Lim, J.Y. Cho, H. Yang, H.-S. Kim, Approach to determine the density-of-states effective mass with carrier concentration-dependent seebeck coefficient, Adv. Funct. Mater. 32 (33) (2022) 2203852.

[55] Y. Lei, J. Qiu, R. Liu, Y. Li, F. Gao, C. Yong, R. Wan, H. Hu, Enhanced thermoelectric figure of merit in indium and ytterbium double-filled skutterudite bulk materials through simultaneously optimising power factor and reducing thermal conductivity, J. Eur. Ceram. Soc. 43 (8) (2023) 3370–3375.